

RESEARCH

2dSpAn-Auto - Spine Analysis Software for two-dimensional dendritic spine images

Shauvik Paul^{2,4†}, Rahul Pramanick^{2†}, Nirmal Das³, Ewa Baczyńska^{1,7}, Tapabrata Chakraborti^{5,6}, Subhadip Basu² and Jakub Włodarczyk^{1*}

*Correspondence:

j.włodarczyk@nencki.edu.pl

¹Nencki Institute of Experimental Biology, Polish Academy of Sciences, Pasteur 3, 02-093 Warsaw, Poland

Full list of author information is available at the end of the article

†Equal contributor

Abstract

Background Quantitative analysis of dendritic spine morphology is crucial for understanding synaptic plasticity and its role in neuropsychiatric disorders, including Alzheimer's disease and schizophrenia. While both 3D and 2D approaches exist for spine analysis, 2D methods offer advantages in computational efficiency and rapid assessment. We developed a data-independent spine segmentation approach based on 2D skeletonization. The method enables automated batch processing while maintaining user flexibility through an intuitive graphical interface. Expert users can fine-tune parameters when needed, though default settings prove robust across various imaging conditions. Following the approach, we developed 2dSpAn-Auto, a novel automated software tool for dendritic spine segmentation and morphological analysis using 2D maximum intensity projections.

Results 2dSpAn-Auto was validated across multiple imaging modalities (*in vitro*, *ex vivo*, and *in vivo*). The software automatically quantifies key morphological metrics including spine density, spine length, head width, neck dimensions, and total dendrite length. Validation studies demonstrate high accuracy in these measurements across different imaging protocols and experimental conditions.

Conclusions 2dSpAn-Auto provides a robust, interpretable solution for quick dendritic spine analysis, addressing a critical need in neurological research and clinical assessment. The combination of automated processing with optional expert oversight makes it suitable for both routine analysis and specialized research applications. The software, complete with source code and comprehensive documentation, is freely available to the research community.

Keywords: Bioimaging; Image processing; Microscopy; Electron microscopy; Segmentation; Dendritic spine images

Introduction

Specialized neuronal extensions called dendrites emerge from the soma and are the main locations where synaptic input is integrated. Dendritic spines, which are tiny membranous protrusions that make up the postsynaptic compartments of the majority of excitatory synapses in the central nervous system, are a distinguishing characteristic of dendrites [1]. The morphology of these spines is varied, including mushroom, thin, stubby, and filopodia-like forms[2]. The structural integrity of dendritic spines is preserved by a dynamic actin cytoskeleton, which also contains important postsynaptic elements including scaffolding proteins, neurotransmitter receptors, and postsynaptic density (PSD)[3]. Many neurological and psychiatric

conditions, such as schizophrenia [4], autism spectrum disorders [5], and Alzheimer's disease [6], are associated with changes in the density and shape of the spine. Accurate measurement and examination of the physical characteristics of dendritic spines are crucial due to their pivotal involvement in neuronal functions and diseases [7].

However, significant technological obstacles exist due to their complicated structure and microscopic scale. The two main methodological approaches used in modern dendritic spine analysis are direct analysis of 3D imaging data [8] and analysis of 2D maximum intensity projections (MIP) obtained from 3D acquisitions [9]. Although 3D analysis of dendritic spine images enables us to achieve greater accuracy in quantitative morphological analysis, these approaches are infeasible for many high-throughput applications due to their substantial computational resources, processing time, and visualization complexity issues. The literature documents numerous approaches for direct 3D microscopic image analysis, including commercial solutions like Imaris [10] that enable four-dimensional spine analysis, these tools often prioritize population-level metrics over individual spine characterization. Janoos et al. proposed [11] a 3D spine reconstruction method using 3-D skeletonization. However, computing 3D skeletons from low-resolution microscopic images is error-prone and not suitable for accurate morphological analysis of individual spines. The automated 4D analysis framework proposed by Swanger and colleagues [12], followed a similar pipeline to Imaris and suffered from similar limitations. Other 3-D pipelines worth mentioning for 3D spine segmentation and analysis can be found in [13], [14]. Basu et al. [8] proposed 3D segmentation method using a multiscale opening algorithm for segmentation and analysis of individual dendritic spine. The method achieved high accuracy in quantitative morphological analysis of individual dendritic spines with the help of expert user interaction.

2D MIP images suffer from structural overlapping and information loss, and it is difficult to analyze accurate individual spine morphology from 2D MIP images. However, on numerous occasions, researchers have used 2D images for quick quantitative morphological analysis of overall spine populations from a large set of dendritic spine images with limited resources. Basu et al. in [9], presented a waterflow-based method for user-interactive segmentation and quantitative morphometric analysis of individual dendritic spines. Ruszczycki et al. [15, 16] proposed a contour tracing algorithm for segmenting and analyzing individual spines. The algorithm requires marking two points per spine—one at the base and one at the head—and setting segmentation parameters. This process becomes labour-intensive in images with high spine density. Like all other fields of imaging, deep learning methods are being recently used for identification, segmentation and analysis of dendritic spine [17, 18]. Although modern deep learning systems are a powerful tool for achieving automatic feature representations, these systems often operate as context-incongruent black boxes, since they are entirely data-driven [19]. The main challenge in deep learning for this domain is the lack of annotated data, as dense dendritic spine regions are difficult to label at a microscopic scale. Moreover, beyond high accuracy, real-world clinical adoption requires transparent decision-making and alignment with biomedical insights.

Several software tools have been developed over the past decade for dendritic spine morphological analysis. We have evaluated and compared these tools, with

the results summarized in the Result Section. We introduce **2dSpAn-Auto**, an automated method for dendritic spine segmentation and analysis in 2D MIP images, integrated into interactive software. The approach leverages 2D skeletonization and key-point identification for precise morphological analysis. It supports batch processing with predefined parameters for efficiency while allowing expert users to fine-tune settings.

The key contributions of this work are:

- 1 An automated, data-independent, and interpretable spine segmentation method based on 2D skeletonization.
- 2 **2dSpAn-Auto**, enabling one-click batch processing with tunable parameters.
- 3 Computation of key morphological metrics: spine length, density, dendrite length, head width, and neck dimensions, validated across multiple imaging modalities (*in vitro*, *ex vivo*, *in vivo*).
- 4 Open-source availability of **2dSpAn-Auto** [available here](#).

Next, we present the mathematical framework and software architecture, followed by experimental validation, discussion, and conclusions.

Methods

In this section, we will discuss the proposed method and the designed software's GUI together. We will discuss the different software modules one by one and their related theories. The graphical user interface (GUI) of the software is shown in Figure 1. The software implements a systematic pipeline comprising three main modules, each addressing specific aspects of spine analysis. The software consists of three primary modules: 1. Image Pre-processing (M1), 2. Dendrite Extraction & Spine Compartmentalization (DESC) (M2), and 3. Morphological Analyser (MorphoAnalyser) (M3).

The module M1 is the essential image pre-processing step before the actual segmentation and analysis pipeline. It consists of two sub-modules: Image denoising and Image binarization. The second module M2, named DESC, represents the core segmentation component of the software. It is structured into two distinct sub-modules: Dendrite Extraction, which isolates the main dendritic structures, and Spine Compartmentalization, which identifies and segments individual spine regions. The final module M3, named MorphoAnalyser, performs a comprehensive quantitative morphological analysis of the segmented spine regions and provides statistical insights about spine characteristics. This module serves as the analytical endpoint of the pipeline and extracts meaningful biological measurements from the processed image. The 2dSpAn-Auto is designed with a modular architecture that distinctly separates the image analysis from the image processing functionalities provided by the software. Different modules and sub-modules with their interconnections are shown in **Supplementary Section 1**. The complete workflow diagram of 2dSpAn-Auto is shown in Figure 2. The M1 module, consisting of denoising and binarization, gives users several options, advanced and traditional algorithms, to choose for optimal preprocessing results. Although preprocessing is a crucial step, the details of the algorithms are given in **Supplementary Section 2** to keep the main text concise and focused on the core analysis method. Even after optimal binarisation, it is often seen that the neck of spines gets detached from their dendritic shaft resulting in the

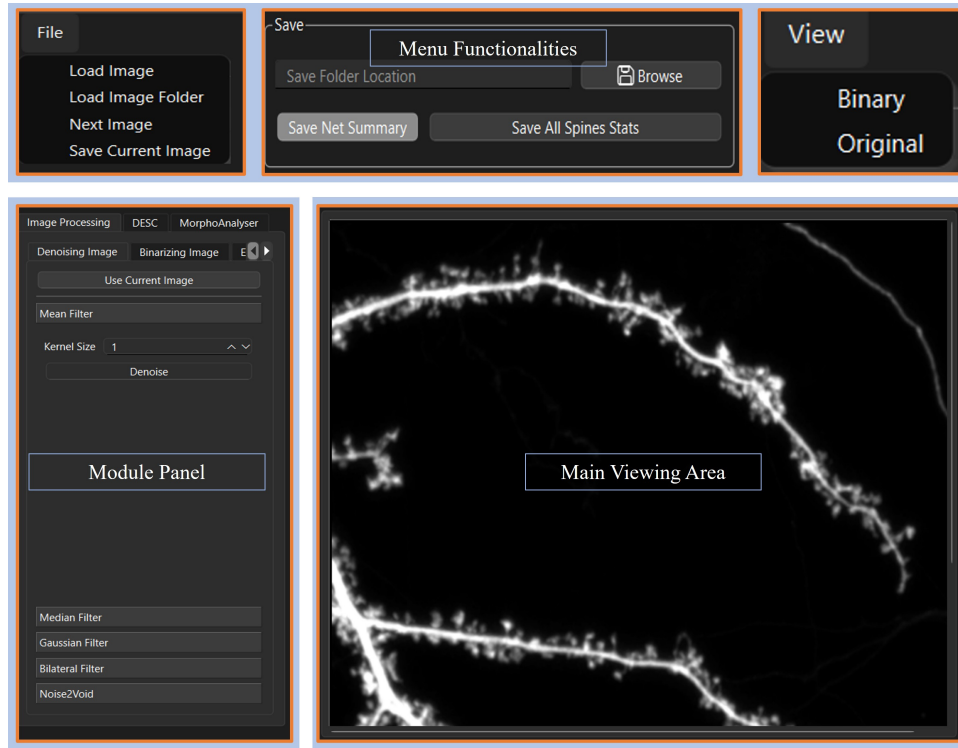


Figure 1: GUI of 2dSpAn-Auto Software. Different sections of the software are shown.

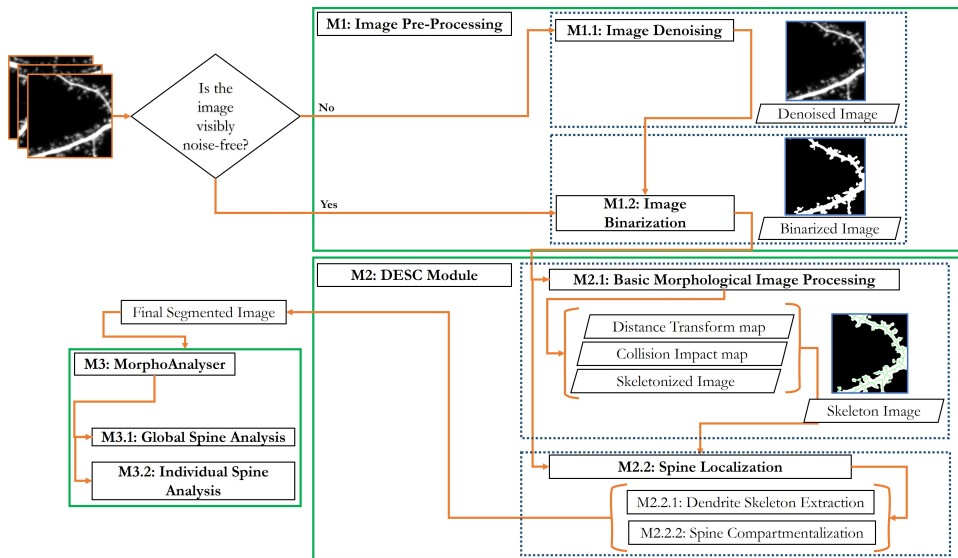


Figure 2: Complete workflow diagram of 2dSpAn-Auto Software

appearance of blob-like shapes. To simplify the image analysis, ignoring these blobs is followed in our software using a module named Spurious Spot and Blob Removal which is explained in **Supplementary Section 2**. After the processing, the final binarised image (Figure 3.b) is shown in Figure 3 for the grayscale image (Figure 3.a).

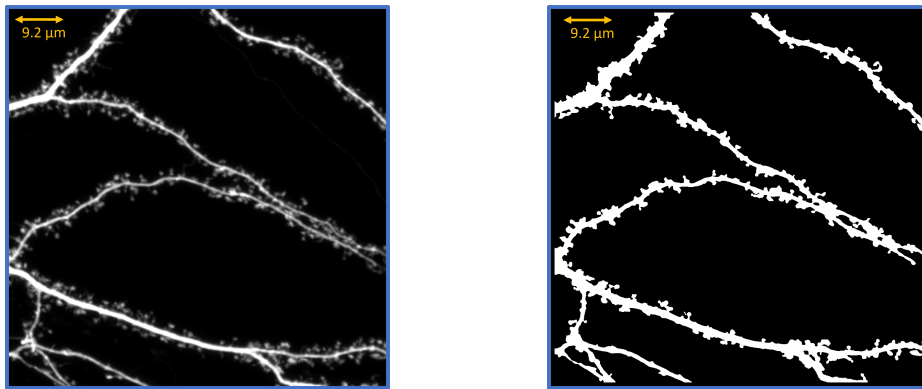


Figure 3: Binarization of a sample dendritic spine image. (a) Original grayscale image, (b) Binarized image.

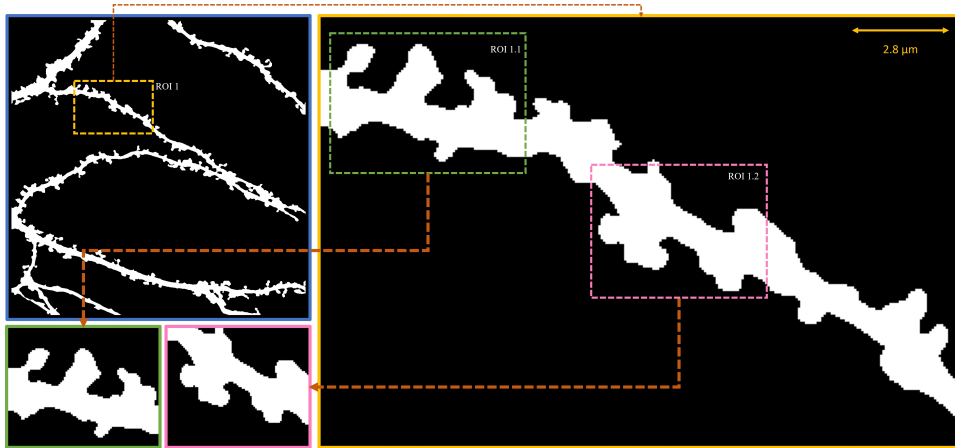


Figure 4: Different ROIs of a binary dendritic spine image. First, an ROI is selected from the main image and then two sub-ROIs are further selected from that ROI. All the ROIs are shown in the zoomed-in version.

Dendrite Extraction And Spine Compartmentalization (**DESC**)

The DESC module constitutes the core component of 2dSpAn-Auto, processing the binarized image to extract critical morphological key points. The module implements a sequential pipeline comprising three primary stages: Skeletonization, Dendrite Extraction(DE), and Spine Compartmentalization (SC). From this point forward, we will demonstrate the effects of various upcoming methods on the previously shown binary image and its selected regions of interest (ROIs) shown in Figure 4.

Skeletonization

Skeletonization is a widely used technique that produces a one-pixel-wide representation of an image while preserving its topology. Various algorithms exist [20], and we adopted the method from [21], originally designed for fuzzy images but modified for binary images. The key components of this approach are briefly discussed below.

Distance Transform For a binary image I , the distance transform(**DT**)[22] at any foreground pixel p is defined as:

$$DT(p) = \min_{q \in B} \{d(p, q)\} \quad (1)$$

where B represents background pixels and $d(p, q)$ is the weighted distance metric.

Blum's Grass Fire Algorithm Computes the collision impact map C based on wavefront propagation:

$$C(p) = \begin{cases} t_c, & \text{if wavefronts collide at } p \\ 0, & \text{otherwise} \end{cases} \quad (2)$$

where t_c represents the collision time of propagating wavefronts[23].

Simple Points A point p is simple[24] if its removal preserves topology, requiring:

- 1 One connected component in $N_8(p) \cap I$
- 2 One connected component in $N_8(p) \cap \bar{I}$
- 3 $N_8(p) \cap I \neq \emptyset$
- 4 $N_8(p) \cap \bar{I} \neq \emptyset$

Given the preceding concepts and definitions, we can formally define the skeleton $S(I)$ of the binary image I as the following set:

$$S(I) = \{p \in I \mid p \in T^n(I) \wedge DT(p) \text{ is locally maximal} \wedge C(p) > 0\} \quad (3)$$

where, $T^n(I)$ represents the result of n iterations of thinning operations preserving simple points. $C(p)$ is the collision impact value from Blum's grassfire propagation

This set definition encapsulates the essential properties of a skeleton:

- (i) Unit width: $\forall p \in S(I), \exists! q \in N_8(p) \cap S(I)$
- (ii) Homotopy: $\chi(S(I)) = \chi(I)$
- (iii) Centrality: $\forall p \in S(I), DT(p)$ is locally maximal

The skeletonization of a binary ROI is shown in Figure 5.

Dendrite Extraction (**DE**)

The sub-module involves the segmentation of the dendritic shaft skeleton, $D(I)$, from the skeletonized representation $S(I)$. The dendrite extraction process is summarized in Figure 6. The dendrite extraction is achieved using three principal steps:

1. Detection of Skeleton Segment Endpoints (**SSE**) and Junction Points (**JP**), 2. Path deletion from **SSE** to nearest **JP**, and 3. Elimination of isolated **JP** or skeleton points.
- Let us first define the key terms:

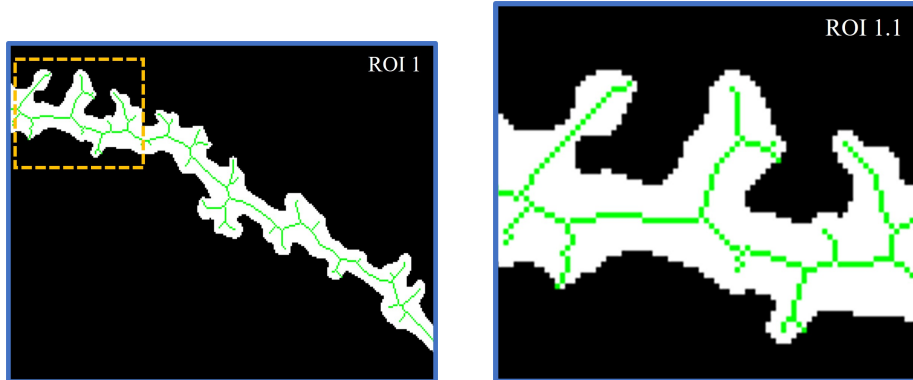


Figure 5: Skeletonization of a binary ROI a) Skeleton on ROI 1. b) Skeletonization on zoomed ROI 1.1

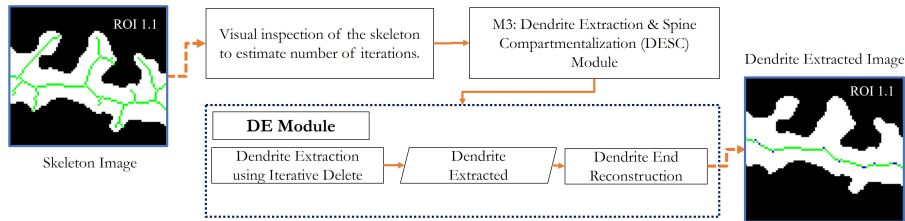


Figure 6: Workflow of DE module is shown using a sample binary ROI(ROI 1.1). It takes the full skeleton image as input and gives the extracted dendrite skeleton as output.

Skeleton Segment Endpoints (SSE) For a given skeleton $S(I)$, a point $p \in S(I)$ is classified as a Spine Segment Endpoint if it satisfies either of the following conditions:

$$p \in \text{SSE} \iff \begin{cases} |N_8(p) \cap S(I)| = 1 & \text{(single neighbor)} \\ \text{or} \\ |N_8(p) \cap S(I)| = 2 \text{ and } L(p) = 1 & \text{(L-configuration)} \end{cases} \quad (5)$$

where $N_8(p)$ represents the 8-neighborhood of point p , and $L(p)$ is an indicator function that equals 1 if the two neighbors form an L-configuration, and 0 otherwise.

Henceforth, we also similarly define spine segment endpoints and will use the term SSE interchangeably to refer to spine segment endpoints in later uses.

L-Configuration For a point $p \in S(I)$, we define the L-configuration indicator function $L(p)$ as:

$$L(p) = \begin{cases} 1, & \text{if } |N_8(p) \cap S(I)| = 2 \text{ and} \\ & (|N_4(p) \cap S(I)| = 1 \text{ and } |N_d(p) \cap S(I)| = 1) \\ 0, & \text{otherwise} \end{cases} \quad (6)$$

where, $N_d(p)$ represents the set of diagonal neighbors of point p in the 8-neighborhood. $N_d(p) = N_8(p) \setminus N_4(p)$

Junction Points (JP) A point $p \in S(I)$ is classified as a Junction Point if:

$$p \in \text{JP} \iff |N_8(p) \cap S(I)| \geq 3 \quad (7)$$

Figure 7 shows the SSE and JP on a sample ROI. These formal definitions provide the mathematical foundation for identifying critical structural elements within the neuronal skeleton, enabling subsequent dendrite shaft segmentation. Let $P(s, j)$ denote the set of skeleton points forming the shortest path from a skeleton segment endpoint $s \in \text{SSE}$ to its nearest junction point $j \in \text{JP}$. If the length of the path $L(P(s, j)) \leq \alpha \cdot \text{DT}(j)$, then $P(s, j)$ is considered for deletion, we write $\text{Near}(P(s, j)) = 1$, otherwise $\text{Near}(P(s, j)) = 0$. The path deletion process is defined iteratively as follows: For each iteration k ,

$$S_{k+1}(I) = S_k(I) \setminus \bigcup_{\substack{s \in \text{SSE}_k \\ \text{Near}(P(s, j_s))=1}} P(s, j_s) \quad (8)$$

where j_s represents the nearest junction point to s , and $S_0(I)$ is the initial skeleton.

After each path deletion, junction points are re-evaluated:

$$\text{JP}_{k+1} = \{p \in \text{JP}_k \mid |N_8(p) \cap S_k(I)| \geq 3\} \quad (9)$$

Junction points that no longer satisfy the connectivity criterion are reclassified:

$$\text{SSE}_{k+1} = \{p \in \text{JP}_k \mid |N_8(p) \cap S_{k+1}(I)| = 1 \mid (|N_8(p) \cap S_{k+1}(I)| = 2 \text{ and } L(p) = 1)\} \quad (10)$$

The process continues until no further reclassification occurs:

$$\text{JP}_{k+1} = \text{JP}_k \text{ and } \text{SSE}_{k+1} = \text{SSE}_k \quad (11)$$

The iterative delete process is applied in Figure 8. JPs are redundant, prompting the need for redundant JP elimination. Four iterations are depicted in Figure 8. Iterative deletion is an effective method but requires post-processing of the output obtained as discussed in **Supplementary Section 3**. The iterative deletion process may result in the loss of skeletal points near dendrite endpoints. To recover these lost dendrite shaft segments, we perform a secondary reconstruction process, named **Dendrite End Reconstruction (DER)**. To keep the overall theory compact, we do not discuss the DER method here. The DER method and its importance are explicitly discussed in **Supplementary Section 4**. After identifying the dendrite shaft, the process transitions to the next module.

Spine Compartmentalization (SC)

Given the dendrite skeleton shaft $D(I) \subseteq S(I)$ obtained from the previous module, we define the set of spine points $Sp(I)$ as:

$$Sp(I) = S(I) \setminus D(I) \quad (12)$$

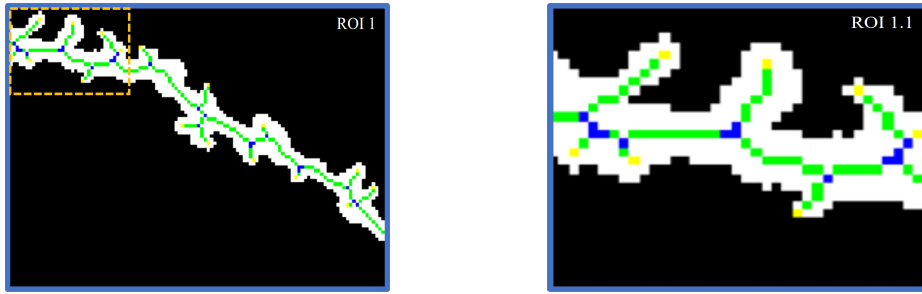


Figure 7: Spine segment end points(yellow) and Junction points(blue) are shown. (Left) Spine segment endpoints and Junction points on ROI 1, (Right) Spine segment endpoints and Junction points on ROI 1.1.

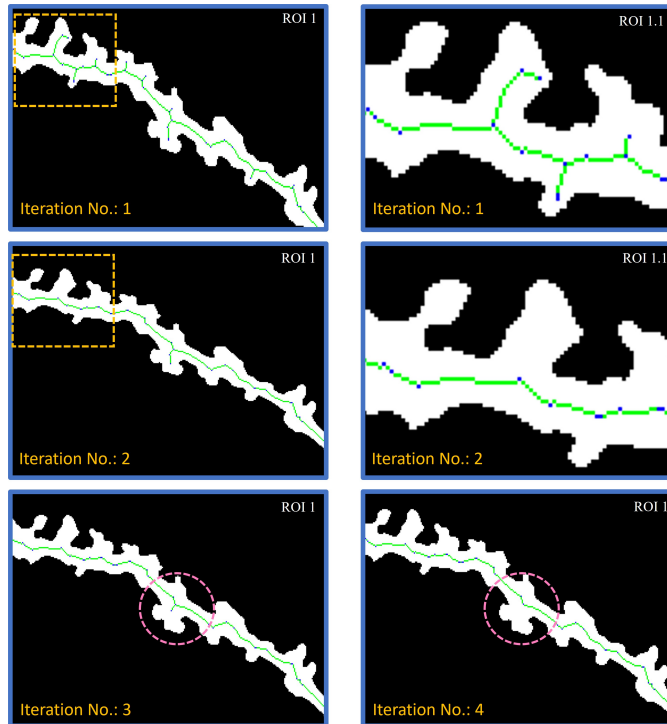


Figure 8: Different Iterations of the iterative delete process for extracting dendrite skeleton.

The details of spine compartmentalization are presented in **Supplementary Section 5**. To facilitate spine analysis, we establish specialized junction classifications:

Dendrite-Dendrite Junction (DDJ) A point $p \in D(I)$ is classified as a DDJ if:

$$p \in \text{DDJ} \iff |N_8(p) \cap D(I)| \geq 3 \quad (13)$$

Spine-Spine Junction (SSJ) A point $p \in Sp(I)$ is classified as an SSJ if:

Let $C(p)$ denote the connectivity of a point p , defined as:

$$C(p) = \{q \in N_8(p) \mid q \in Sp(I) \cup \text{SSE} \cup \text{SSJ} \cup \text{JP} \cup \text{DDJ}\} \quad (14)$$

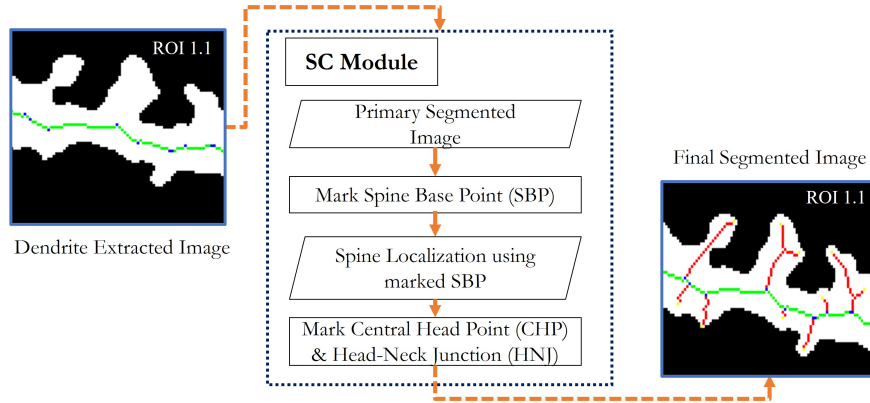


Figure 9: The workflow of SC module is shown on ROI 1.1. Extracted dendrite skeleton image is the input to the SC module and segmented dendrite and spine skeleton is the output.

$$p \in \text{SSJ} \iff |C(p)| \geq 3 \quad (15)$$

The workflow in Figure 9 summarizes the SC process.

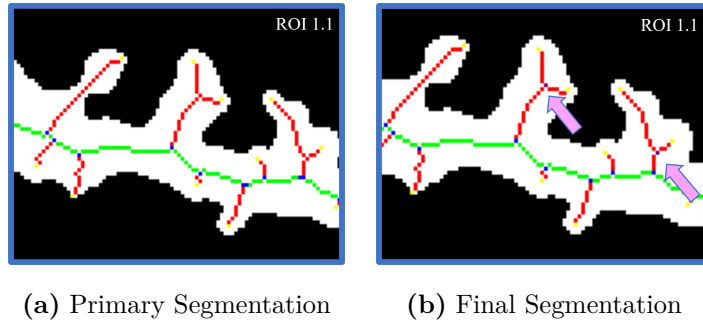


Figure 10: **Dendritic Spine Segmentation Process.** (a) Initial segmentation of the skeletal structure, highlighting the distinction between preliminary spine components and the dendrite shaft. The yellow points denote SSE points. (b) The final segmentation result includes identifying SSJ points, and facilitating further morphological analysis, with purple points representing SSJ points.

The primary segmentation in Figure 10 establishes a foundation for systematically decomposing the skeletal structure into distinct spine components while preserving their topological relationships with the dendrite shaft. This approach also facilitates further segmentation based on specific morphological characteristics.

Following this step, the next objective is to mark these crucial markers namely, *Spine Base Point (SBP)*, *Central Head Point (CHP)*, and *Head Neck Junction Point (HNJ)* to facilitate the next module in computing statistical data effectively.

Spine Base Point (SBP) Detection For each junction or dendrite endpoint $p \in \text{JP} \cup \text{DDJ} \cup \text{DEnd}$, we define the set of Spine Base Points $\text{SBP}(p)$ as follows:

$$S(p) = \beta \cdot \text{DT}(p) \quad (16)$$

where, β is a tunable parameter and $S(p)$ represents the required path length from p . Let $\mathcal{P}(p)$ be the set of all paths in $Sp(I)$ originating from p . Then:

$$\text{SBP}(p) = \{q \in Sp(I) \mid \exists \text{ path } P \in \mathcal{P}(p) : \text{length}(P) = S(p), q = P_{\text{end}}\} \quad (17)$$

This formulation effectively identifies the intersection points between $Sp(I)$ and a circle of radius $S(p)$ centred at p . An SBP is thus a unique identifier of a spine. SBPs are marked in Figure 11.

Central Head Point (CHP) Detection Detecting Central Head Points requires analysis of local maxima in the DT space over the spine mass. The process comprises two primary steps. Those steps are discussed in **Supplementary Section 6**.

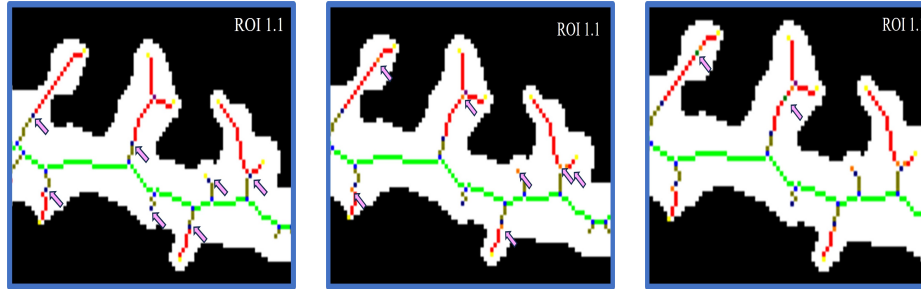


Figure 11: (Left) SBPs are detected in the final segmented image and marked. (Center) Pixels in orange depict the CHP of that spine. (Right) The above image shows HNJ when κ is set minimally. The dark green pixel shows the position of HNJs of their respective non-FILOPODIA spines.

The steps ensure accurate spine mass consideration and robust Central Head Point detection through skeletal analysis and centroid computation.

Head Neck Junction (HNJ) Detection First, we establish criteria for filopodia identification using statistical measures of the DT values:

$$\sigma_p = \sqrt{\frac{1}{|S(\text{FSM}(p))|} \sum_{q \in S(\text{FSM}(p))} (\text{DT}(q) - \mu_p)^2} \quad (18)$$

where, μ_p is the mean DT value over $S(\text{FSM}(p))$, σ_p is the standard deviation. The set of filopodia is then defined as:

$$\text{FILOPODIA} = \{p \in \text{SBP} \mid \sigma_p < \theta_\sigma \text{ or } \kappa_p < \theta_\kappa\} \quad (19)$$

where θ_σ and θ_κ are tunable thresholds.

For non-filopodia spines ($p \notin \text{FILOPODIA}$), the Head Neck Junction is defined as:

$$\text{Head Radius } (\text{HR})(p) = \kappa \cdot \text{DT}(\text{CHP}(p)) \quad (20)$$

where κ is a tunable parameter. Let $P(\text{CHP}(p), p)$ be the path from $\text{CHP}(p)$ to p . Then:

$$\text{HNJ}(p) = \begin{cases} q \in P(\text{CHP}(p), p), & \text{if } d(q, \text{CHP}(p)) = \text{HR}(p) \text{ and } q \text{ precedes } p \\ p, & \text{if } d(p, \text{CHP}(p)) \leq \text{HR}(p) \text{ (stubby spine)} \end{cases} \quad (21)$$

where $d(x, y)$ represents the path distance between points x and y .

This formulation accommodates both regular spines and the special case of stubby spines where the HNJ coincides with or cannot extend beyond the SBP. At this stage, all essential topological markers necessary for morphological spine analysis are in place.

MorphoAnalyser

The MorphoAnalyser module computes morphological metrics utilizing the topological markers (CHP, SBP, HNJ) established in previous modules. The module quantifies key spine characteristics based on definitions established in [8].

Let \mathcal{S} denote the set of all spines, where each spine $s \in \mathcal{S}$ is characterized by its markers: $s = \{\text{CHP}_s, \text{SBP}_s, \text{HNJ}_s\}$

The module comprises two primary analytical components:

1. Individual Spine Statistics For each spine s , we compute the following morphological quantities: Head Width ($\text{HW}(s)$), Spine Length ($\text{SL}(s)$), Minimum Neck Width ($\text{MNW}(s)$), Average Neck Width ($\text{ANW}(s)$), Area ($\text{A}(s)$)

2. Global Summarised Statistics For the complete image I : $\overline{\text{HW}} = \frac{1}{|\mathcal{S}|} \sum_{s \in \mathcal{S}} \text{HW}(s)$, $\overline{\text{SL}} = \frac{1}{|\mathcal{S}|} \sum_{s \in \mathcal{S}} \text{SL}(s)$, $\overline{\text{MNW}} = \frac{1}{|\mathcal{S}|} \sum_{s \in \mathcal{S}} \text{MNW}(s)$, $\overline{\text{ANW}} = \frac{1}{|\mathcal{S}|} \sum_{s \in \mathcal{S}} \text{ANW}(s)$, $\overline{\text{A}} = \frac{1}{|\mathcal{S}|} \sum_{s \in \mathcal{S}} \text{A}(s)$

Additional metrics include: DL = Dendrite Length, SD = $\frac{|\mathcal{S}|}{\text{DL}}$ (Spine Density)

Results

In this section, we evaluate our spine analysis framework through several key objectives. In this study, we evaluated our method using three distinct categories of dendritic spine images, *in vitro*, *ex vivo*, and *in vivo* microscopy data. Our analysis encompassed two experimental conditions: chemically-induced Long-Term Potentiation (cLTP) and its control counterpart, Dimethyl Sulfoxide (DMSO). The imaging protocols and experimental procedures for all three modalities have been thoroughly documented in our previous work [25].

Result on ROI 1 Table 1 contains the spine data obtained from the software on ROI 1. Figure 12 shows the spine numbering.

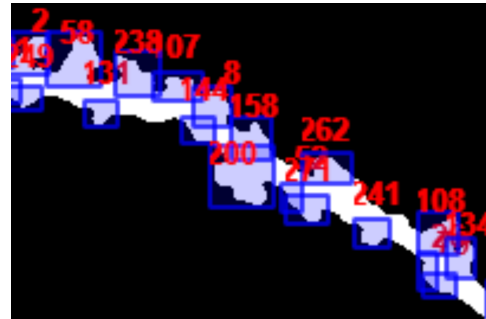


Figure 12: ROI 1 with all spines numbered

Table 1: Morphological characteristics of dendritic spines

Spine ID	Type	HW (μm)	NL (μm)	SL (μm)	ANW (μm)	MinNW (μm)	MaxNW (μm)	Area (μm^2)
2	Mushroom	0.28	0.35	0.90	0.29	0.00	0.41	0.60
111	Mushroom	0.62	0.14	1.38	0.40	0.00	0.41	0.22
249	Stubby	0.35	0.00	0.69	0.00	0.00	0.00	0.23
58	Mushroom	0.83	0.14	1.79	0.43	0.00	0.41	1.03
131	Stubby	0.48	0.00	0.97	0.00	0.00	0.00	0.27
238	Stubby	0.69	0.00	1.38	0.00	0.00	0.00	0.49
107	Stubby	0.55	0.00	1.10	0.00	0.00	0.00	0.48
8	Stubby	0.83	0.00	1.66	0.00	0.00	0.00	0.43
144	Stubby	0.55	0.00	1.10	0.00	0.00	0.00	0.24
158	Stubby	0.62	0.00	1.24	0.00	0.00	0.00	0.49
200	Mushroom	1.04	0.28	2.35	0.54	0.00	0.62	1.46
262	Stubby	0.83	0.00	1.66	0.00	0.00	0.00	0.59
271	Stubby	0.69	0.00	1.38	0.00	0.00	0.00	0.40
241	Stubby	0.62	0.00	1.24	0.00	0.00	0.00	0.30
108	Mushroom	0.69	0.41	1.79	0.34	0.00	0.41	0.57
26	Mushroom	0.69	0.14	1.52	0.38	0.00	0.41	0.21
79	Stubby	0.83	0.00	1.66	0.00	0.00	0.00	0.22
134	Stubby	0.48	0.00	0.97	0.00	0.00	0.00	0.35

HW: Head Width; NL: Neck Length; SL: Spine Length; ANW: Average Neck Width; MinNW: Minimum Neck Width; MaxNW: Maximum Neck Width. All measurements are in micrometers (μm) except Area which is in square micrometers (μm^2).

Comprehensive Morphological Analysis

We present quantitative measurements of key spine morphological parameters for three sample images from different imaging protocols in Table 2 and provide a visual comparison of the segmentation results. The results presented here and onwards were obtained using the software's default parameters to ensure consistency across outcomes. This section presents the results obtained from analyzing characteristic spines in an Ex-Vivo cell image given in Figure 13.c using our software. Table 3 and corresponding Figure 14 highlight key spine characteristics, such as type, head width, neck length, and spine length, for selected stubby and mushroom spines.

This section presents the results of analyzing characteristic spines in an In-Vitro cell image given in Figure 13.b using our software. Similarly, Table 4 highlights key spine characteristics, such as type, head width, neck length, and spine length, for selected stubby and mushroom spines.

Table 2: Dendritic Spine Morphology Across Different Imaging Modalities

Characteristic	Parameter	ExVivo	InVitro	InVivo
Overall Distribution	Total Spines	324	178	593
	Stubby	202	94	106
	Mushroom	122	84	487
Stubby Spines	Avg. HW	0.58 ± 0.70	0.99 ± 1.20	4.18 ± 2.13
	Avg. SL	1.16 ± 1.40	1.98 ± 2.40	8.36 ± 4.26
	Avg. Area	14.07 ± 11.96	26.04 ± 35.23	35.30 ± 22.85
Mushroom Spines	Avg. HW	1.02 ± 0.85	0.96 ± 0.98	4.61 ± 1.74
	Avg. NL	2.47 ± 1.00	3.85 ± 3.05	4.01 ± 2.34
	Avg. SL	4.52 ± 2.14	5.77 ± 3.56	13.24 ± 4.87
	Avg. NW	1.09 ± 0.72	1.04 ± 0.68	6.64 ± 2.55
	Avg. Area	23.74 ± 21.48	41.61 ± 34.25	99.47 ± 93.60

Values are presented as mean \pm standard deviation. All measurements are in pixels for dimensions and square pixels (pixel 2) for areas. Avg. means average, HW means Head Width, SL means Spine Length, NL means Neck Length, NW means Neck Width.

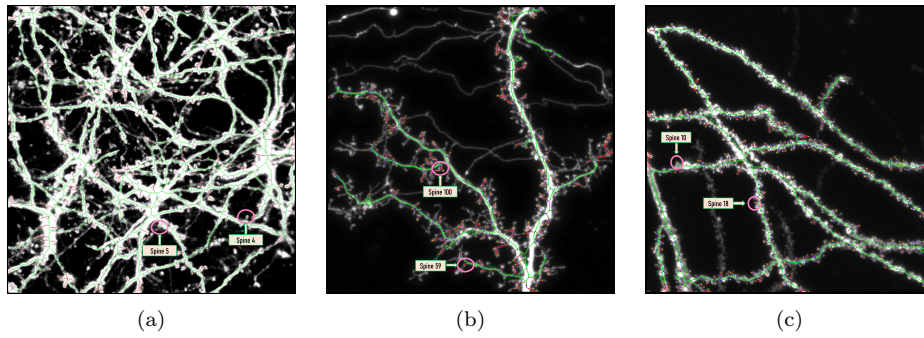


Figure 13: Representative images showing dendritic spines in different modalities:
(a) In-Vivo cell, (b) In-Vitro cell, and (c) Ex-Vivo cell.

Depiction of Characteristic Spines in In-Vivo Cell Image This section presents the results of analyzing characteristic spines in an In-Vivo cell image given in Figure 13.a using our software. Similarly, Table 5 highlights key spine characteristics, such as type, head width, neck length, and spine length, for selected stubby and mushroom spines.

Comparative Performance Analysis Evaluating the accuracy of different modalities on the region of interest (ROI) is crucial for assessing their reliability in various applications. This analysis compares the performance of multiple imaging techniques on ROI accuracy with an expert's measurement. We have experimented on multiple spine images and observed an average spine detection accuracy of approximately 71.787%. The software demonstrated an accuracy of approximately 70% in calculating morphological quantities, as experimentally verified on synthetic images with precisely known dimensions. Figure 15, Table 6,7 illustrates the ROI accuracy for Ex-Vivo data. In Figure 15, the original grayscale image contained 34 spines, whereas the segmented image detected 24 spines, resulting in a spine detection accuracy of 70.588%.

Figure 16, Table 8,9 illustrates the ROI accuracy for In-Vitro data. In Figure 16, the original grayscale image contained 34 spines, whereas the segmented image detected 28 spines, resulting in a spine detection accuracy of 82.353%.

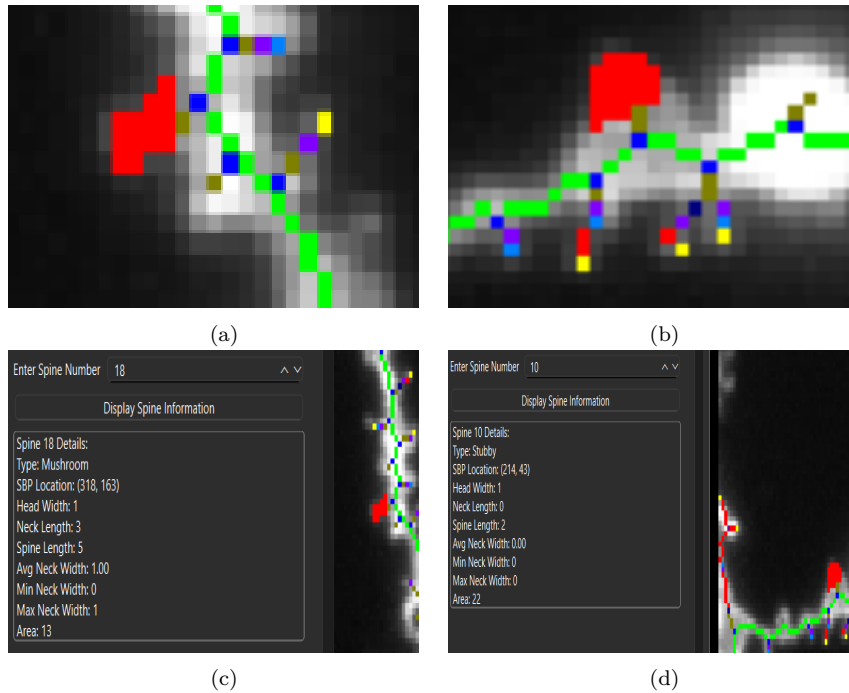


Figure 14: A close view of the segmented Ex-Vivo image is presented here. (a) represents the segmented spine no. 18 and (c) represents its statistics.(b) represents the segmented spine no. 10 and (d) represents its statistics.

Table 3: Spine Characteristics Table of ExVivo Image given in Figure 13.c

Id	Type	SBP X	SBP Y	HW	NL	SL	ANW	MNW	MaNW	Area
10	Stubby	214	43	0.069	0.0	0.138	0.0	0.0	0.0	1.518
18	Mushroom	318	163	0.069	0.207	0.345	0.069	0.0	0.069	0.897

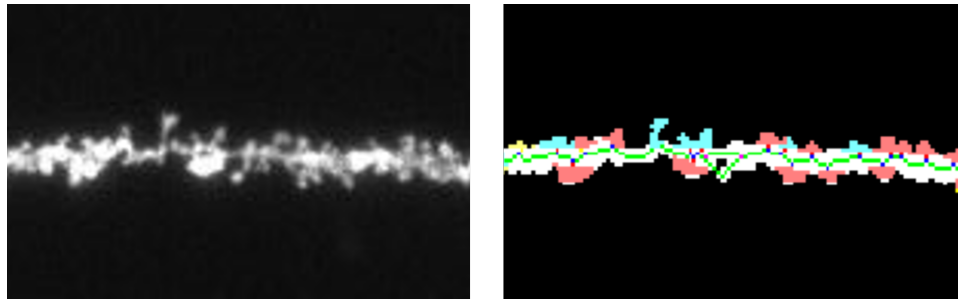


Figure 15: The original and segmented Ex-Vivo ROI images

Figure 17, Table 10,11 illustrates the ROI accuracy for In-Vivo data. In Figure 17, the original grayscale image contained 20 spines, whereas the segmented image detected 13 spines, resulting in a spine detection accuracy of 68.421%.

Plasticity Analysis of spines in both cLTP and DMSO Plasticity analysis of dendritic spines is crucial for understanding synaptic modifications underlying learning and memory. Chemical long-term potentiation (cLTP) induces structural and functional changes in spines, mimicking synaptic strengthening, while dimethyl sulfoxide

Table 4: Spine Characteristics Table of In Vitro Image given in Figure 13.b

Id	Type	SBP X	SBP Y	HW	NL	SL	ANW	MNW	MaNW	Area
59	Stubby	366	241	0.069	0.000	0.138	0.000	0.000	0.000	1.035
100	Mushroom	217	154	0.138	0.207	0.483	0.115	0.000	0.069	2.760

Table 5: Spine Characteristics Table of In-Vivo Image given in Figure 13.a

Id	Type	SBP X	SBP Y	HW	NL	SL	ANW	MNW	MaNW	Area
4	Mushroom	481	496	0.207	0.138	0.552	0.219	0.000	0.207	2.898
5	Stubby	137	722	0.345	0.000	0.690	0.000	0.000	0.000	1.863

Table 6: Individual Spine Morphological Measurements

Index	Type	Head Width	Neck Length	Spine Length	Neck Width (μm)			Area
		(μm)	(μm)	(μm)	Avg	Min	Max	
0	Mushroom	0.138	0.138	0.414	0.184	0.000	0.207	1.035
1	Filopodia	0.000	0.000	0.069	0.000	0.000	0.000	0.552
2	Stubby	0.276	0.000	0.552	0.000	0.000	0.000	1.035
3	Stubby	0.207	0.000	0.414	0.000	0.000	0.000	1.035
4	Stubby	0.483	0.000	0.966	0.000	0.000	0.000	1.242

Table 7: Global Spine Morphology Statistics by Type

Parameter	Filopodia	Stubby	Mushroom
	Mean \pm SD	Mean \pm SD	Mean \pm SD
Head Width (μm)	0.00 \pm 0.00	4.53 \pm 1.31	3.71 \pm 3.06
Neck Length (μm)	0.00 \pm 0.00	0.00 \pm 0.00	3.14 \pm 1.73
Spine Length (μm)	1.00 \pm 0.00	9.07 \pm 2.62	10.57 \pm 7.33
Avg Neck Width (μm)	0.00 \pm 0.00	0.00 \pm 0.00	2.50 \pm 0.86
Area (μm^2)	9.50 \pm 1.50	19.00 \pm 6.03	42.86 \pm 40.22
Distribution (n=24)	2	15	7

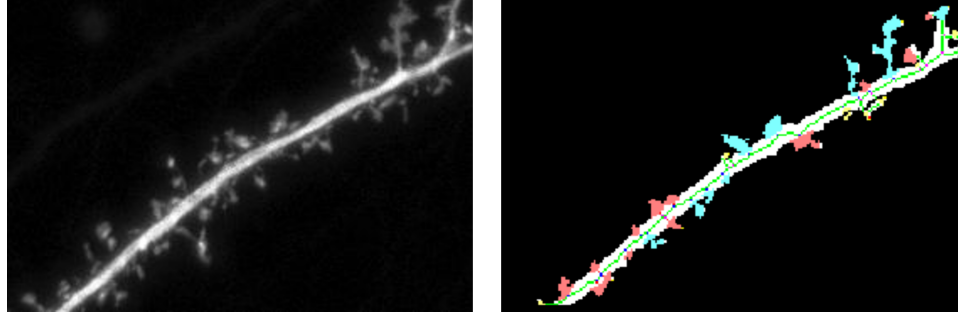


Figure 16: The original and segmented In-Vitro ROI images

Table 8: Individual Spine Morphological Measurements

Index	Type	SBP X	SBP Y	Head Width	Neck Length	Spine Length	Neck Width (μm)			Area
		(μm)	(μm)	(μm)	(μm)	(μm)	Avg	Min	Max	
0	Filopodia	28	188	0.000	0.000	0.069	0.000	0.000	0.000	0.207
1	Stubby	41	166	0.414	0.000	0.828	0.000	0.000	0.000	1.311
2	Mushroom	60	123	0.552	0.138	1.242	0.264	0.000	0.276	3.864
3	Mushroom	88	94	0.138	0.138	0.414	0.184	0.000	0.207	1.518
4	Mushroom	44	161	0.000	0.690	0.690	0.055	0.000	0.069	3.450

(DMSO) serves as a control. Comparing spine dynamics in both conditions helps elucidate mechanisms of synaptic plasticity and potential experimental artefacts. Table 12 presents the analysis of two cell images using our software: one cLTP and one DMSO, both at the time stamp $t = 10$ units. These images were selected for

Table 9: Global Spine Morphology Statistics by Type

Parameter	Filopodia	Stubby	Mushroom
	Mean \pm SD	Mean \pm SD	Mean \pm SD
Head Width (μm)	0.00 \pm 0.00	4.64 \pm 1.29	3.40 \pm 2.42
Neck Length (μm)	0.00 \pm 0.00	0.00 \pm 0.00	4.50 \pm 3.91
Spine Length (μm)	2.33 \pm 1.41	9.29 \pm 2.58	11.30 \pm 5.60
Avg Neck Width (μm)	0.00 \pm 0.00	0.00 \pm 0.00	2.17 \pm 0.81
Area (μm^2)	6.56 \pm 3.13	28.71 \pm 17.01	48.20 \pm 33.01
Distribution (n=33)	9	14	10

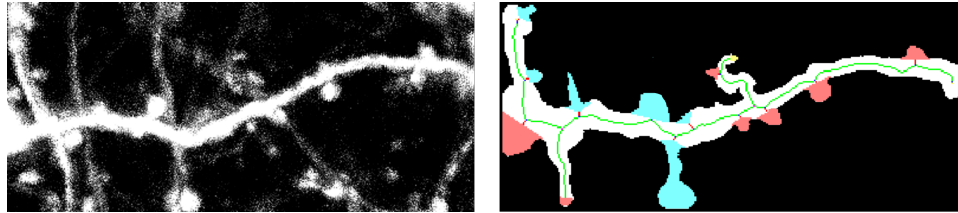


Figure 17: Comparison of the original and segmented In-Vivo images

Table 10: Individual Spine Morphological Measurements

Index	Type	SBP X	SBP Y	Head Width (μm)	Neck Length (μm)	Spine Length (μm)	Neck Width (μm)			Area (μm^2)
							Avg	Min	Max	
0	Stubby	128	72	0.828	0.000	1.656	0.000	0.000	0.000	8.349
1	Stubby	6	48	0.690	0.000	1.380	0.000	0.000	0.000	3.588
2	Stubby	203	73	1.035	0.000	2.070	0.000	0.000	0.000	26.841
3	Stubby	180	90	0.828	0.000	1.656	0.000	0.000	0.000	2.622
4	Mushroom	96	55	0.966	0.552	2.484	0.426	0.000	0.483	11.109

Table 11: Global Spine Morphology Statistics by Type

Parameter	Stubby	Mushroom
	Mean \pm SD	Mean \pm SD
Head Width (μm)	11.95 \pm 1.82	12.00 \pm 4.24
Neck Length (μm)	0.00 \pm 0.00	11.00 \pm 7.75
Spine Length (μm)	23.89 \pm 3.64	35.00 \pm 11.18
Avg Neck Width (μm)	0.00 \pm 0.00	6.63 \pm 1.74
Area (μm^2)	107.42 \pm 77.87	359.00 \pm 279.96
Distribution (n=27)	19	8

comparison due to their closely matching population scales, ensuring a meaningful evaluation. As expected, cLTP exhibits enhanced feature values compared to DMSO, highlighting its impact on synaptic plasticity.

Visual Comparison of Segmentation Results This section provides a qualitative evaluation of the final segmentation results produced by our software. The images presented here compare the original image, its binary segmentation output, and the segmentation overlay on the grayscale image. This allows for a visual assessment of the accuracy and effectiveness of the segmentation process. Figure 18 presents an original grayscale image, the segmentation result on the binarized image and the corresponding segmentation result on the original grayscale image.

Comparison of various existing 2D spine morphological analysis softwares Several software tools have been developed over the past decade for dendritic spine morphological analysis. We have evaluated and compared these tools, with the results summarized in Table 13.

Table 12: Comparison of Dendritic Spine Characteristics between cLTP and DMSO Conditions

Category	Parameter	DMSO	cLTP
Overall	Total Spines	404	269
	Filopodia (%)	0.99	3.35
	Stubby (%)	54.46	59.85
	Mushroom (%)	44.55	36.80
Filopodia	Spine Length (μm)	2.25 ± 0.43	1.78 ± 0.63
	Area (μm^2)	5.25 ± 2.05	4.78 ± 2.10
Stubby	Head Width (μm)	9.33 ± 2.64	8.21 ± 2.26
	Spine Length (μm)	18.66 ± 5.28	16.42 ± 4.51
	Area (μm^2)	86.71 ± 54.96	66.30 ± 39.25
Mushroom	Head Width (μm)	8.62 ± 3.57	7.05 ± 3.48
	Neck Length (μm)	3.36 ± 2.67	4.10 ± 3.11
	Spine Length (μm)	20.59 ± 7.53	18.20 ± 7.39
	Neck Width (μm)	6.60 ± 2.81	5.01 ± 2.34
	Area (μm^2)	123.89 ± 100.84	113.02 ± 79.16

Note: Values are presented as mean \pm standard deviation where applicable. Percentages for spine types are calculated relative to total spine count.

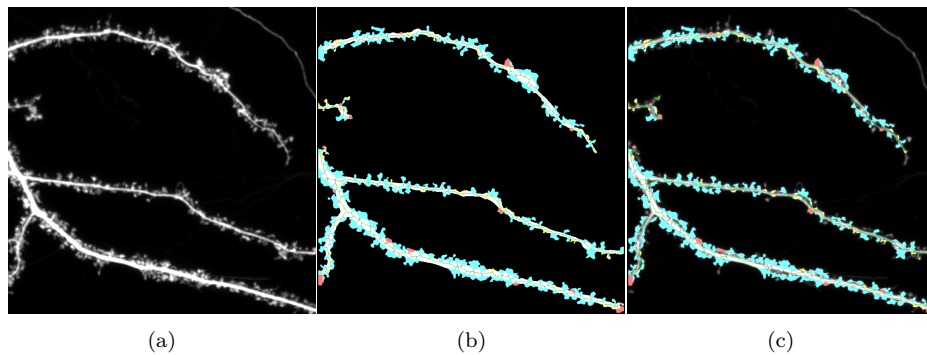


Figure 18: Mushrooms are marked in blue, Stubby are marked in red, Filopodia are marked in yellow. This is an image of a cLTP cell at $t=0$.

Discussions

The 2dSpAn-Auto software, while effective for dendritic spine analysis, encounters several challenges across its various processing stages. The main challenge arises from the MIP image itself, due to structure overlap and loss of contextual information. The preprocessing module (M1) is crucial for the next module to work properly and for the software's overall performance. The denoising module includes several filtering methods to balance feature preservation and noise reduction. Image binarization poses another significant challenge, as the process can inadvertently fragment or completely sever spine necks if the thresholding parameters are not optimal. In both cases, an expert user can manipulate the parameters to obtain desired

Table 13: Comparison of 2D Dendritic Spine Analysis Software Tools

results through visual inspection. The subsequent removal of spurious spots, while necessary for clean analysis, can result in the loss of potentially relevant structural information. We conducted experiments with varying thresholds and analyzed their impact on the final results(See **Supplementary Section 7.**)

The dendrite extraction process, implemented through iterative deletion, faces a few limitations. The method struggles to reliably differentiate between spine endpoints and dendrite endpoints, leading to potential misclassification of structural elements. The purely topological approach fails to incorporate the contextual understanding that human experts apply when identifying dendrite structures. Spine reconstruction faces particular challenges at the spine-dendrite interface, where accurately defining the boundary between these structures becomes problematic due to the complex three-dimensional nature of their interaction being projected onto a two-dimensional plane. This interface ambiguity can affect spine length and neck width measurements, particularly in cases where the spine base merges gradually with the dendrite shaft.

Finally, the classification of spines presents a fundamental statistical challenge. Developing orientation, size, and scale-invariant encodings of spine morphology, necessary for consistent classification and comparison across different imaging conditions and samples, remains an open problem. This limitation impacts the reliability of automated spine type classification, particularly in borderline cases where spines exhibit characteristics of multiple morphological categories.

These challenges, while not invalidating the utility of the 2dSpAn-Auto approach, underscore the importance of careful parameter tuning and expert validation in specific applications, particularly in studies where precise morphological classifications or measurements are critical to the research conclusions.

Conclusions

In summary, the present work provides a data-independent, traditional, and fully interpretable method of automatic dendritic spine segmentation and morphometric analysis method. Also, we designed a freely available 2dSpAn-Auto software implementing the proposed method for the neuroimaging community. The source code is also available to download. In the result section we have that 2dSpAn-Auto is computationally efficient and provides robust morphological analysis results across different imaging protocols like *in vitro*, *ex vivo*, and *in vivo*. In future, instead of rule-based spine classification, we may incorporate advanced machine learning or deep learning models for better classification results.

Supporting information

For further read, please refer to **Supplementary Section 7.**

Acknowledgements

This work is partially supported by the CMATER research laboratory of the Computer Science and Engineering Department, Jadavpur University, India and Nencki Institutue of Experimental Biology, Warsaw, Poland. S.B. acknowledges Department of Biotechnology grant (BT/PR16356/BID/7/596/2016) along with Science and Engineering Research Board grant(SUR/2022/002903), Government of India. T.C. is supported by the Turing-Roche Strategic Partnership.

Author details

¹Nencki Institute of Experimental Biology, Polish Academy of Sciences, Pasteur 3, 02-093 Warsaw, Poland.
²Department of Computer Science and Engineering, Jadavpur University, Raja Subodh Chandra Mallick Rd 188, 700032 Kolkata, India. ³Department of CSE(AIML), Institute of Engineering and Management, Management House, D-1, Sector-V, Saltlake Electronics Complex, 700091 Kolkata, India. ⁴Department of IT, Techno Main Saltlake, EM-4/1, Sector V, 700091 Kolkata, India. ⁵Health Sciences Programme, The Alan Turing Institute, London, UK. ⁶Department of Medical Physics and Biomedical Engineering, University College London, London, UK. ⁷Department of Regenerative Medicine, Maria Skłodowska-Curie National Research Institute of Oncology, Roentgenna 5, 02-781 Warsaw, Poland.

References

1. Segal, M.: Dendritic spines and long-term plasticity. *Nature Reviews Neuroscience* **6**(4), 277–284 (2005)
2. Jones, E., Powell, T.: Morphological variations in the dendritic spines of the neocortex. *Journal of cell science* **5**(2), 509–529 (1969)
3. Rao, A., Craig, A.M.: Signaling between the actin cytoskeleton and the postsynaptic density of dendritic spines. *Hippocampus* **10**(5), 527–541 (2000)
4. Glausier, J.R., Lewis, D.A.: Dendritic spine pathology in schizophrenia. *Neuroscience* **251**, 90–107 (2013)
5. Hutsler, J.J., Zhang, H.: Increased dendritic spine densities on cortical projection neurons in autism spectrum disorders. *Brain research* **1309**, 83–94 (2010)
6. Knobloch, M., Mansuy, I.M.: Dendritic spine loss and synaptic alterations in alzheimer's disease. *Molecular neurobiology* **37**, 73–82 (2008)
7. Penzes, P., Cahill, M.E., Jones, K.A., VanLeeuwen, J.-E., Woolfrey, K.M.: Dendritic spine pathology in neuropsychiatric disorders. *Nature neuroscience* **14**(3), 285–293 (2011)
8. Basu, S., Saha, P.K., Roszkowska, M., Magnowska, M., Baczyńska, E., Das, N., Plewczynski, D., Włodarczyk, J.: Quantitative 3-d morphometric analysis of individual dendritic spines. *Scientific reports* **8**(1), 3545 (2018)
9. Basu, S., Plewczynski, D., Saha, S., Roszkowska, M., Magnowska, M., Baczyńska, E., Włodarczyk, J.: 2dspan: semiautomated 2-d segmentation, classification and analysis of hippocampal dendritic spine plasticity. *Bioinformatics* **32**(16), 2490–2498 (2016)
10. Wörbs, T., Förster, R.: 4d-tracking with imaris. Bitpl.-Oxford Instruments (2007)
11. Janoos, F., Mosaliganti, K., Xu, X., Machiraju, R., Huang, K., Wong, S.T.: Robust 3d reconstruction and identification of dendritic spines from optical microscopy imaging. *Medical image analysis* **13**(1), 167–179 (2009)
12. Swanger, S.A., Yao, X., Gross, C., Bassell, G.J.: Automated 4d analysis of dendritic spine morphology: applications to stimulus-induced spine remodeling and pharmacological rescue in a disease model. *Molecular brain* **4**, 1–14 (2011)
13. Rodriguez, A., Ehlenberger, D.B., Hof, P.R., Wearne, S.L.: Rayburst sampling, an algorithm for automated three-dimensional shape analysis from laser scanning microscopy images. *Nature protocols* **1**(4), 2152–2161 (2006)
14. Rodriguez, A., Ehlenberger, D.B., Dickstein, D.L., Hof, P.R., Wearne, S.L.: Automated three-dimensional detection and shape classification of dendritic spines from fluorescence microscopy images. *PloS one* **3**(4), 1997 (2008)
15. Ruszczycki, B., Włodarczyk, J., Kaczmarek, L.: Method and a system for processing an image comprising dendritic spines. Google Patents. US Patent App. 14/237,352 (2014)
16. Ruszczycki, B., Szepesi, Z., Wilczynski, G.M., Bijata, M., Kalita, K., Kaczmarek, L., Włodarczyk, J.: Sampling issues in quantitative analysis of dendritic spines morphology. *BMC bioinformatics* **13**, 1–12 (2012)
17. Vidaurre-Gallart, I., Fernaud-Espinosa, I., Cosmin-Toader, N., Talavera-Martínez, L., Martín-Abadal, M., Benavides-Piccione, R., González-Cid, Y., Pastor, L., DeFelipe, J., García-Lorenzo, M.: A deep learning-based workflow for dendritic spine segmentation. *Frontiers in neuroanatomy* **16**, 817903 (2022)
18. Fernholz, M.H., Guggiana Nilo, D.A., Bonhoeffer, T., Kist, A.M.: Deepd3, an open framework for automated quantification of dendritic spines. *PLOS Computational Biology* **20**(2), 1011774 (2024)
19. ŞAHİN, E., Arslan, N.N., Özdemir, D.: Unlocking the black box: an in-depth review on interpretability, explainability, and reliability in deep learning. *Neural Computing and Applications*, 1–107 (2024)
20. Saha, P.K., Borgefors, G., di Baja, G.S.: A survey on skeletonization algorithms and their applications. *Pattern recognition letters* **76**, 3–12 (2016)
21. Saha, P.K., Borgefors, G., di Baja, G.S.: Skeletonization and its applications—a review. *Skeletonization*, 3–42 (2017)
22. Borgefors, G.: Distance transformations in digital images. *Computer vision, graphics, and image processing* **34**(3), 344–371 (1986)
23. Liu, L., Chambers, E.W., Letscher, D., Ju, T.: Extended grassfire transform on medial axes of 2d shapes. *Computer-Aided Design* **43**(11), 1496–1505 (2011)
24. Saha, P.K., Chaudhuri, B.B.: Detection of 3-d simple points for topology preserving transformations with application to thinning. *IEEE Transactions on Pattern Analysis and Machine Intelligence* **16**(10), 1028–1032 (1994). doi:[10.1109/34.329007](https://doi.org/10.1109/34.329007)
25. Das, N., Baczyńska, E., Bijata, M., Ruszczycki, B., Zeug, A., Plewczynski, D., Saha, P.K., Ponimaskin, E., Włodarczyk, J., Basu, S.: 3dspan: An interactive software for 3d segmentation and analysis of dendritic spines. *Neuroinformatics*, 1–20 (2022)
26. Pchitskaya, E., Vasiliev, P., Smirnova, D., Chukanov, V., Bezprozvanny, I.: Spinetool is an open-source software for analysis of morphology of dendritic spines. *Scientific reports* **13**(1), 10561 (2023)
27. Levet, F., Tønnesen, J., Nägerl, U.V., Sibarita, J.-B.: Spinej: A software tool for quantitative analysis of nanoscale spine morphology. *Methods* **174**, 49–55 (2020)
28. Choi, J., Lee, S.-E., Lee, Y., Cho, E., Chang, S., Jeong, W.-K.: Dxplorer: a unified visualization framework for interactive dendritic spine analysis using 3d morphological features. *IEEE Transactions on Visualization and*

- Computer Graphics **29**(2), 1424–1437 (2021)
29. Gilles, J.-F., Mailly, P., Ferreira, T., Boudier, T., Heck, N.: Spot spine, a freely available imagej plugin for 3d detection and morphological analysis of dendritic spines. F1000Research **13**, 176 (2024)